

Embedded Stellar Populations towards Young Massive Star Formation Regions I. G305.2+0.2

S. N. Longmore^{1,2*}, M. Maercker³, S. Ramstedt³, M.G. Burton^{1,4}

¹*School of Physics, University of New South Wales, Kensington, 2052, Sydney, Australia*

²*Australia Telescope National Facility CSIRO, Epping, Sydney, NSW 1710, Australia*

³*Stockholm Observatory, AlbaNova University Center, 106 91 Stockholm, Sweden*

⁴*Armagh Observatory, College Hill, Armagh, BT61 9DG*

ABSTRACT

We present deep, wide-field J, H and Ks images taken with IRIS2 on the Anglo Australian Telescope, towards the massive star formation region G305.2+0.2. Combined with 3.6, 4.5, 5.8 and 8.0 μm data from the GLIMPSE survey on the Spitzer Space Telescope, we investigate the properties of the embedded stellar populations. After removing contamination from foreground stars we separate the sources based on their IR colour. Strong extended emission in the GLIMPSE images hampers investigation of the most embedded sources towards the known sites of massive star formation. However, we find a sizeable population of IR excess sources in the surrounding region free from these completeness effects. Investigation reveals the recent star formation activity in the region is more widespread than previously known.

Stellar density plots show the embedded cluster in the region, G305.24+0.204, is offset from the dust emission. We discuss the effect of this cluster on the surrounding area and argue it may have played a role in triggering sites of star formation within the region. Finally, we investigate the distribution of IR excess sources towards the cluster, in particular their apparent lack towards the centre compared with its immediate environs.

Key words: infrared:stars, stars:early-type, open clusters and associations:general, stars:evolution, stars:formation, stars:pre-main sequence, stars:kinematics.

1 INTRODUCTION

Reprocessing of stellar light by circumstellar material around young stars is observed at infrared (IR) wavelengths as excess emission above that of a blackbody. The extent of the IR excess provides a measure of the amount of circumstellar material and hence an indication of the evolutionary state of the object (e.g. Adams et al. 1987). Traditionally, the J, H and K bands (1.2, 1.6 and 2.2 μm) have successfully been used to identify IR excess sources (e.g. Lada & Adams 1992) but recent work including L-band (3.6 μm) data has highlighted that IR-excess sources are much more clearly separated using longer wavelengths (Kenyon & Hartmann 1995; Maercker & Burton 2005; Maercker et al. 2006). With large optical depths of material towards the youngest regions, mid-IR observations at high enough spatial resolution to resolve individual sources are required to uncover the most heavily embedded objects (e.g. Longmore et al. 2006). By combining deep, wide-field, near-IR images of selected regions with catalogued mid-IR data, we aim to identify IR-

excess sources, uncover their spatial distribution and investigate the star formation history of the regions. For this first paper, we have chosen a region which has also been studied on the same telescope with near-IR spectroscopy of selected objects (Leistra et al. 2005). Using these, we can calibrate our derived photometric spectral types and so compare results from the automated matching routines to check their accuracy.

1.1 The G305 complex

The $\sim 1.5^\circ \times 1.5^\circ$ region at $l \sim 305^\circ$ within the Scutum-Crux arm of the galaxy, designated G305 by Georgelin et al. (1988), is a large ($\sim 100\text{pc}$ in extent) complex of recent and active star formation at a distance of between 3.3 and 4kpc (Leistra et al. 2005). With an age of 3-5 Myr, the complex is one of the most luminous giant HII regions in the galaxy containing in excess of 31 O stars. Clark & Porter (2004) have recently summarised the global properties of the complex which include two optically revealed clusters, several embedded IR clusters, significant HII emission, many UCHII regions and sites of maser emission (see Clark & Porter (2004)

* E-mail: snl@phys.unsw.edu.au

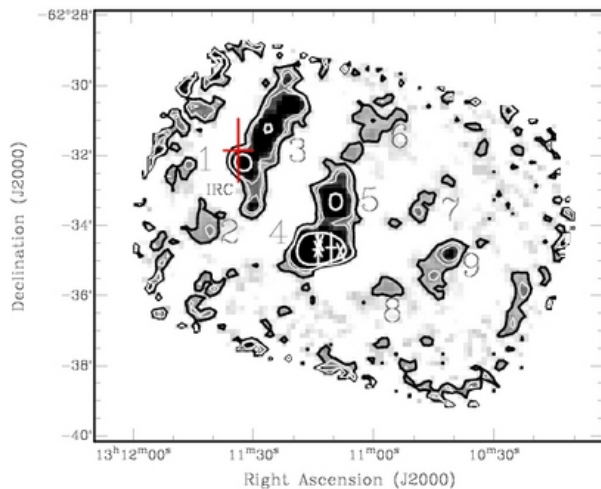


Figure 1. 1.2mm dust continuum map of the G305.20+0.2 region (from Hill et al. 2005) overlaid with black contours at 5σ and white contours at 10, 15 and 50σ levels. The letters ‘IRC’ show the position of the infrared cluster, G305.24+0.204. Plus and cross symbols show the position of methanol and water masers respectively. Regions of emission are numbered 1 to 9 and designated MM1, MM2 etc. for future reference. The apparent emission at the edge of the image are artefacts from the mapping process.

for references and further details). Evidence suggests that the optically revealed clusters (Danks 1 & 2) and associated Wolf-Rayet star (WR 48a) are driving a wind-blown bubble surrounding the entire region, which is responsible for triggering a second generation of star formation – the embedded near-IR clusters – towards the edge of the bubble. This includes the cluster G305.24+0.204, on the NW edge, which contains several late O/early B stars (Leistra et al. 2005) that are only apparent at IR wavelengths. Figure 1 shows the 1.2mm continuum emission (from Hill et al. 2005) in the vicinity of this cluster (the position of which is labelled as ‘IRC’) and shows several dust emission regions. The brightest 1.2mm core (MM4 in Figure 1) has previously been studied from the near-IR (De Buizer 2003) through mid-IR (Walsh et al. 2001), mm continuum (Hill et al. 2005), mm molecular line (Walsh & Burton 2006), 6.67GHz Class II methanol maser emission (Norris et al. 1993) and cm continuum (Phillips et al. 1998; Walsh 2002). These observations reveal both ultra-compact HII regions and even younger massive stellar sources within the core, suggesting it harbours a deeply embedded massive proto-cluster. Furthermore, molecular line observations near MM5 and 8 (G305N and G305SW respectively from Walsh & Burton 2006) show the molecular gas to be both cold and quiescent, and as such may be examples of pre-stellar cores. With multiple epochs of star formation in the region, we aim to investigate the recent star formation history by identifying the embedded and youngest sources through their IR colours.

2 IRIS2 OBSERVATIONS AND DATA REDUCTION

The J, H and Ks-band (1.2 , 1.6 and $2.2\mu\text{m}$) images were observed using IRIS2¹ (Infrared Imager and Spectrometer 2) on the 3.9m Anglo Australian Telescope (AAT) at Siding Spring Observatory. The Ks band observations were taken on the 25th of July 2002 and the J/H band observations carried out on the 16th-17th May 2006 with seeing of $1 - 1.2''$. For each source, a 3×3 image grid was created with $\sim 1'$ offsets from the pointing centre. The integration time at each of the nine grid points was around one minute with $3 \times 20\text{s}$, $6 \times 10\text{s}$ and $9 \times 6\text{s}$ exposures at J, H and Ks respectively. The detector bias was removed at read-out time using the Double Read Mode. The data were reduced using the in-house ORAC-DR pipeline with the ‘JITTER_SELF_FLAT_KEEPBAD’ ORAC-DR² recipe to correct for dark current, create flat-field images from star free pixels in the 9 jittered source fields and apply a bad pixel mask to each image. The pipeline then corrects for distortion at the outer edges of the image caused by the slightly curved focal plane. The 9 individual fields of $7.7' \times 7.7'$ were finally aligned and mosaiced together to give a $9.7' \times 9.7'$ field of view, although only the inner $5.7' \times 5.7'$ are covered by all 9 fields. The blind telescope pointing error is estimated to be $\sim 3''$ but absolute coordinates were calculated by comparing non-saturated stars to those in the 2MASS catalogue. Using the *koords* program in the KARMA³ visualisation package, the image coordinates were matched to better than 0.1 pixel accuracy. We take the error in the absolute coordinates to be the error in the 2MASS catalogue of $0.3''$.

The photometry was calibrated from the 2MASS catalogue by plotting the magnitude difference between matched stars as a function of the measured IRIS2 magnitude and the mean offset calculated over a suitable magnitude range (~ 12 to 14). The standard deviation in this range is ~ 0.2 mag but some of this scatter is likely to be due to the difference between the MKO photometric system used by IRIS2 and the 2MASS photometric system⁴. Although converting to the 2MASS photometric system may marginally reduce this scatter, the colour correction terms are not characterised for sources with $(J-H) > 1.5$, $(H-K) > 1$ and $(J-K) > 2$. As we are primarily interested in the sources with reddest colours, the photometry has therefore been left in the MKO system.

Sources were extracted from each of the IRIS2 images using the *daophot* tasks in the IRAF⁵ package to produce a J, H and Ks star catalogue. Examination of the residuals after removing the stellar flux from the image shows the stars have been well extracted despite different background levels across the image (due to varying extended emission) and the crowded field. We found 8667, 11762 and 11226 sources at J, H and Ks band respectively, with a median photometric error from the automated fitting of ~ 0.02 mag. The stars in the individual catalogues with $> 3\sigma$ detections were then

¹ IRIS2 employs a 1024x1024 Rockwell HAWAII-1 HgCdTe infrared detector with a plate scale of $0.4486 \pm 0.0002''$ per pixel.

² see <http://www.oracdr.org>

³ <http://www.atnf.csiro.au/computing/software/karma/>

⁴ See <http://www.astro.caltech.edu/~jmc/2mass/v3/transformations/>

⁵ <http://iraf.noao.edu/>

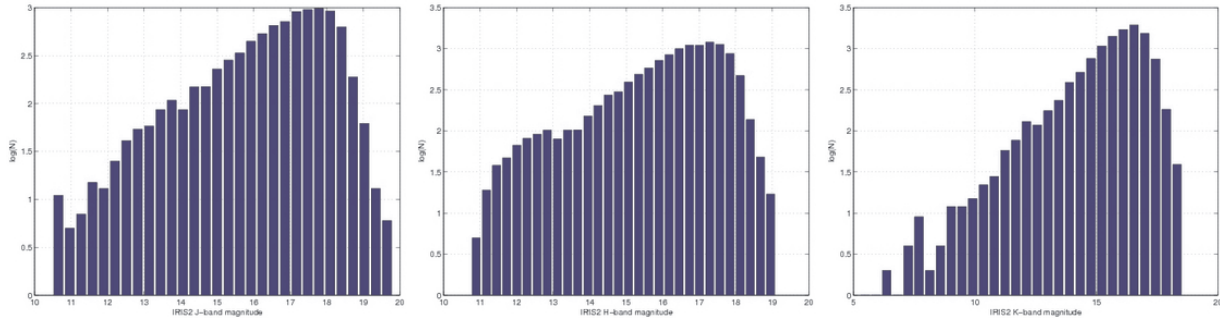


Figure 2. Histograms of the J (left), H (centre) and Ks (right) star magnitudes extracted from the IRIS2 images. The 90% completeness limit from artificial star recovery and maximum measured magnitudes are 18 & 19.8, 17.5 & 19.1, 16.5 & 18.5 at J, H and Ks respectively.

matched as outlined in § 4.1 to produce a final IRIS2 JHKs catalogue⁶.

2.1 Previous IRIS2 observations

The previous IRIS2 observations carried out by Leistra et al. (2005) were also made using the J, H and Ks band filters with a similar integration time and observation method but were instead focused on the cluster centred at $\alpha_{J2000} = 13:11:39.4$, $\delta_{J2000} = -62:33:11$. $R \simeq 2300$ spectra with a $1''$ -wide slit were also taken toward the cluster. Analysis of the spectra and photometry revealed G305.24+0.204 as an OB association with an O5-O6V star and extinction of $A_v \sim 12$ mags.

3 CATALOGUE DATA

3.1 2MASS - 2 micron All Sky Survey

Using two 1.3m telescopes in Arizona and Chile, the 2MASS survey scanned the entire sky at the J, H and Ks bands (1.25 , 1.65 and $2.17\mu\text{m}$) (Skrutskie et al. 2006). The survey has a limiting magnitude of 15.8, 15.1, 14.3 ± 0.03 mag at J, H and Ks respectively with a pixel size of $2.0''$ and $0.1''$ pointing accuracy.

3.2 GLIMPSE - Galactic Legacy Infrared Mid-Plane Survey Extraordinaire

Using the infrared array camera (IRAC) on-board the Spitzer Space Telescope (SST⁷), the GLIMPSE survey has observed the galaxy at 3.6 , 4.5 , 5.8 and $8.0\mu\text{m}$ with a $1.2''$ pixel size between $10^\circ < |l| < 65^\circ$ and $|b| < 1^\circ$ (Benjamin et al. 2003). The photometric accuracy is 0.2 and 0.3 mag for bands 1/2 and 3/4 respectively. The astrometric accuracy of the point source catalogue is $\sim 0.3''$.

4 THE POINT SOURCE CATALOGUE

4.1 Matching sources at different wavelengths

Analysis of source colours relies on the ability to accurately match sources in the catalogues at different wavelengths. With too many sources ($>10^4$) to check manually and crowded stellar fields, there is a potential problem of either matching a source multiple times or mismatching the sources completely. The resulting mismatched sources may replicate the large colour differences of embedded sources and hence contaminate the sample. To test the matching accuracy, we generated and matched synthetic catalogues with known offsets from a list of absolute source positions. In order to ensure a realistic spatial distribution of sources, including over densities due to clustering and under densities due to extinction, the absolute coordinates were taken from the 2MASS PSC of the region. The coordinates recorded in the synthetic catalogues were randomly offset from the absolute values by a 2D Gaussian distribution. Several synthetic catalogues were produced using the known absolute pointing error of the relevant datasets to generate the positional offsets. The sources in the synthetic catalogues were given a unique ID and then matched in the same way as the observed datasets using the *tmatch* routine in the *tables.ttools* package in IRAF. The routine matches every source in the first catalogue with the nearest counterpart in the second catalogue within a user defined matching radius. Comparing the ID of the matched sources in the synthetic catalogues it is possible to unambiguously identify which sources have been matched correctly.

The IRIS2 images were all registered with the same 2MASS image so have a *relative* astrometric uncertainty of $\Delta_{IRIS2} = 0.04''$ (0.1 pixel). The astrometric uncertainty in the 2MASS and GLIMPSE surveys are both quoted as $0.3''$. However, the GLIMPSE survey coordinates were also registered with 2MASS data so the relative uncertainty between the IRIS2 and GLIMPSE catalogues should be considerably less than the assumed error of $\Delta_{IRIS2-GLIMPSE} = 0.3''$. Matching two synthetic catalogues generated with an uncertainty of Δ_{IRIS2} , an equal number of sources and a search radius of 2 pixels, produces a 100% recovery with no confusion due to doubles or mismatches. Matching catalogues generated with an uncertainty of Δ_{IRIS2} but different number of sources also recovers 100% of the sources correctly but includes $\sim 0.05\%$ double sources. With different numbers of sources in each catalogue, the matching order then

⁶ Table 2 shows an extract from the catalogue. The full catalogue will be made available on-line.

⁷ <http://ssc.spitzer.caltech.edu/>

becomes important. For example, matching the catalogue with larger to smaller number of sources may produce ‘multiple matches’, where several sources in the larger catalogue are within the matching radius of a source in the smaller catalogue. However, the number of correctly matched sources is the same, irrespective of the matching order. Varying the matching radius has little effect as long as it is significantly larger than the combined astrometric uncertainty. A matching radius of $1.2''$ was used throughout. We concluded that mismatches do not seriously affect our results.

The IRIS2 PSC was generated by matching the sources found at each wavelength in turn from shortest to longest wavelength. To ensure no red sources were missed, the non-matched sources at the longer wavelength were also appended to the catalogue after each step. The 2MASS PSC of the same region was used to test the colour/magnitudes of the brighter IRIS2 PSC sources. The IRIS2 PSC was then matched with the GLIMPSE PSC to produce the final combined IRIS2/GLIMPSE PSC. A 2MASS/GLIMPSE PSC of the region was also created in a similar way as a comparison. Using this method, we expect to recover at least 99.8% of the sources correctly with a maximum of 0.1% doubles and 0.12% mismatches.

4.2 Completeness

We used artificial star recovery to investigate the spatial variation in point source sensitivity as a function of wavelength. Having calculated the PSF for each image, we inserted a grid of artificial stars of the same magnitude separated by $30''$ across the image. We then used the same automated finding technique outlined in § 2 to calculate how many of the artificial stars were recovered. By shifting the $30'' \times 30''$ grid of artificial stars in small steps through the image, it was possible to measure the completeness at $5''$ intervals without the PSF of individual artificial stars overlapping. The process was repeated by increasing the artificial star magnitudes in steps of 0.5 mag until no more stars were recovered. By recording the largest recovered magnitude at each position and wavelength it was possible to build a three-dimensional picture of the point source sensitivity across the region. The *relative* completeness as a function of position was then calculated at each wavelength by subtracting the median completeness magnitude at that wavelength from every position. This method is similar to that used by Gutermuth (2005) in an analysis of completeness limits of Spitzer IRAC data.

Figure 4 illustrates the spatial variation in completeness for the J, H and Ks images. The contours show the relative completeness at -0.5 , -1.0 , -1.5 and -2.0 mags highlighting the areas with poorest point source sensitivity. Compared to the three colour image in Figure 3a it is clear that although there is some extended emission, particularly at Ks, the main factors contributing to decreased sensitivity are saturated stars, stellar crowding (e.g. the cluster toward the North-East) and the lower integration time at the edge of the images due to mosaicing. Figure 7 shows similar contours at 3.6 and $4.5\mu\text{m}$ over the IRIS2 field of view overlaid on the GLIMPSE images. This time, extended emission is the dominant factor contributing to decreased completeness.

The 90% completeness limit calculated from the artificial star recovery methods above is 18, 17.5 and 16.5 at J,

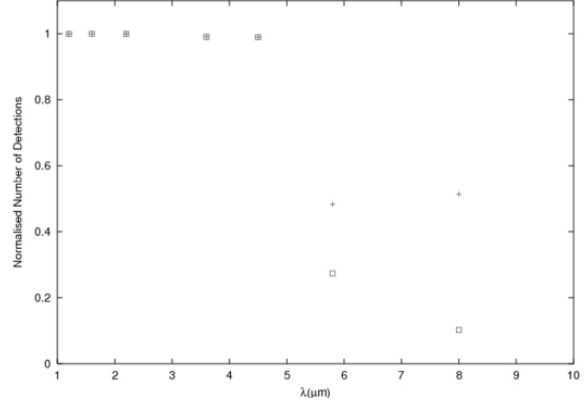


Figure 5. Number of sources detected at each wavelength in the combined 2MASS and GLIMPSE catalogues of the target (square) and control fields (plus symbols) as outlined in § 4.3. The number of sources at each wavelength are normalised to those detected at $1.2\mu\text{m}$.

H and Ks respectively. Figure 2 shows a histogram of the calculated J, H and Ks magnitudes. The turnover in the number of stars per magnitude and faintest measured magnitudes are 17.8 & 19.8, 17.3 & 19.1, 16.6 & 18.5 at J, H and Ks respectively. These limiting magnitudes are fainter than those reported by Leistra et al. (2005) of 16, 18 and 18.5 due to confusion towards the cluster, G305.24+0.204, which was the focus of their observations.

We also note that the turnover is nearly the same as the 90% completeness limit found from the artificial star recovery method. Since it is considerably easier to determine the turnover, it provides a quicker way of estimating the completeness limit.

4.3 Control Field

In order to compare the sources in the target region with a field star population, a nearby region with no extended emission in either the GLIMPSE or 2MASS images (centred at $\alpha_{J2000} = 12:54:10.3$ $\delta_{J2000} = -62:16:12$, $l=303.25$ $b=+0.6$) was chosen as a control field. All sources in the GLIMPSE and 2MASS catalogues within a $9.7' \times 9.7'$ box centred on this position were matched using the same procedure outlined previously. Figure 5 shows the number of sources detected at each wavelength normalised to the number of sources detected at $1.2\mu\text{m}$ for the target (square) and control fields (plus symbols). In both fields, the number of sources matched up to $4.5\mu\text{m}$ is similar with a sharp drop at longer wavelengths, as most field stars are too faint to detect. This is exacerbated in the target field by the extended emission at 5.8 and $8.0\mu\text{m}$. In § 5.1.1 the source colours derived from 2MASS/GLIMPSE for the target and control regions are compared to those derived from the IRIS2/GLIMPSE PSC.

4.4 Nature of the IR excess sources

We aim to use the catalogue to pick out young stellar objects with excess IR emission through their derived colours. However, these highly reddened colours are not unique to young

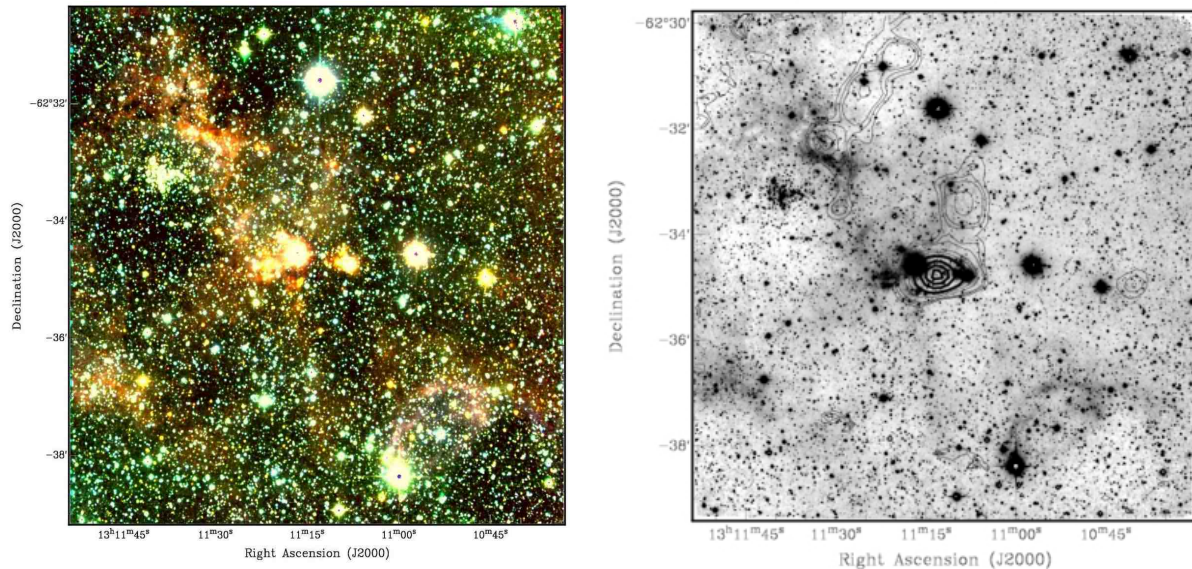


Figure 3. a (Left) Three colour (J, H and Ks) IRIS2 image of the region G305.2+0.2. b (Right) The IRIS2 Ks-band image, overlaid with contours of 1.2mm continuum dust emission from Hill et al. (2005).

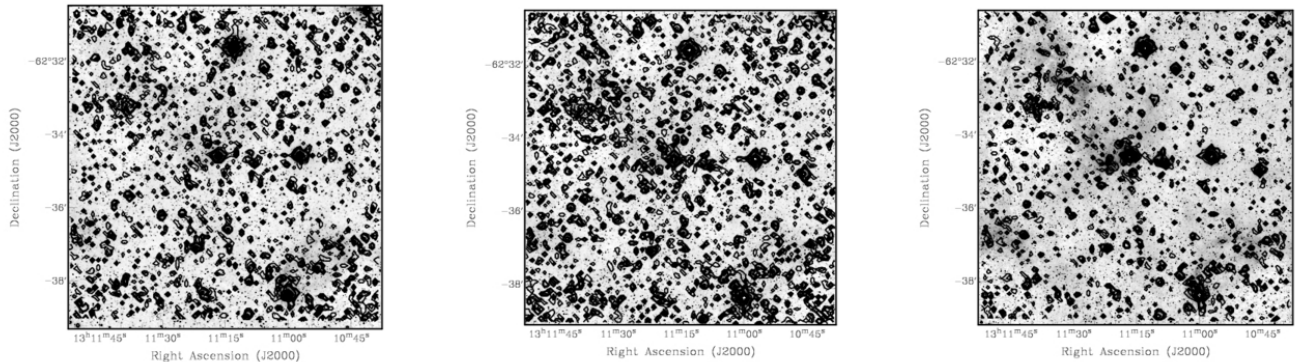


Figure 4. The spatial variation in completeness for the J (left), H (centre) and Ks (right) images calculated as outlined in § 4.2 overlaid on the images at the same wavelengths. The contours show the relative completeness at -0.5, -1.0, -1.5 and -2.0 mags, highlighting the areas with poorest point source sensitivity. An online version in colour illustrates the detail.

stellar objects. We are therefore interested in calculating the likely contamination from other astronomical sources with similar colours – primarily evolved stars and background galaxies.

Recent Spitzer observations toward the LMC show that background galaxies with similar colours to young stellar objects ($[3.6]-[8.0]>1.5$) have the potential to contaminate deep observations for red objects (Blum et al. 2006). It is possible to calculate this likely contamination using the relative number counts of foreground stars to background galaxies as a function of observed magnitude for the IRAC bands reported by Fazio et al. (2004). The galaxy contribution to the source number counts over this wavelength range only becomes significant for magnitudes greater than 14. Given the 90% completeness limit of ~ 14 , 13.5, 11.5 and 11 mags

at 3.6, 4.5, 5.8, $8.0\mu\text{m}$, the background galaxies are too faint to cause contamination.

With luminosities of 10^3 - $10^4 L_\odot$, radiative transfer modelling shows that any asymptotic giant branch (AGB) stars along the line of sight to the edge of the Galaxy will be detected in the IRAC bands (Groenewegen 2006). The same models show that the derived colours, which depend on the mass loss rate of each AGB star, cover the expected colour range for young stellar objects. From photometry alone, it is therefore not trivial to distinguish between AGB stars and young stellar objects. However, with a model distribution of AGB stars in the Galaxy it is possible to predict the expected number of evolved stars within a given field of view. We used the Jackson et al. (2002) model to calculate the number density of AGB stars as a function of Galactic radius and height above the Galactic plane, $|z|$, along our line

of sight. By integrating the product of the number density function with discrete volume elements to the edge of the Galaxy, we then derived the expected number of AGB stars along the line of sight. Assuming a Galactic radius of 15kpc, a distance of 8.5kpc to the Galactic centre and using $|z|=0$ (i.e. looking directly through the Galactic plane) we expect to find ~ 0.7 AGB stars along the line of sight. It is therefore unlikely that this region will suffer from significant evolved star contamination.

5 RESULTS

Figure 3a shows an IRIS2, 3-colour image of the region at near-IR (J, H and Ks) wavelengths and Figure 3b shows the Ks image overlayed with 1.2mm dust continuum emission from Hill et al. (2005) to show the most embedded NIR sources. The image shows lanes of bright extended emission at $2.2\mu\text{m}$ which are seen as red in the 3-colour image. Figure 7 shows the GLIMPSE images of the region at 3.6 and $4.5\mu\text{m}$. The extended emission seen at Ks dominates the 5.8 and $8.0\mu\text{m}$ GLIMPSE images, making point source extraction of all but the brightest sources impossible at these wavelengths. Although the extended emission is seen at 3.6 and $4.5\mu\text{m}$, the images are not affected to the same extent. The nature of the extended emission is consistent with C-C and C-H bending modes of polycyclic aromatic hydrocarbon (PAH) emission at 3.3, 6.2, 7.7 and $8.6\mu\text{m}$ within the bands excited by UV radiation (van Dishoeck 2004). As a result of being unable to extract sources at the longest wavelength towards the previously studied star formation regions we may be missing a population of the most embedded sources.

We find the majority of stars extracted from the catalogues are spread uniformly across the field, except for the region with the 1.2mm dust emission and the extended emission at longer IR wavelengths. The clear exception is the cluster at $\alpha_{J2000}=13:11:39$, $\delta_{J2000}=-62:33:12$, with radius $\sim 45''$, which abuts the northern dust filament. The cluster (G305.24+0.204) has previously been reported by Dutra et al. (2003) as an IR cluster and since been studied in depth by Leistra et al. (2005). We discuss the nature of the cluster and its relation to the surrounding region in section § 5.2.

5.1 Stellar populations

To identify the nature of the sources, we analysed the measured star colours and magnitudes. Figure 8 shows colour-colour (CC) and colour-magnitude (CM) diagrams of all stars in the IRIS2/GLIMPSE PSC matched in the IRIS2 bands. The [J]-[H] vs [H]-[Ks] diagram shows that, while the bulk of the sources are foreground stars, a large fraction are significantly reddened. There are a small number of sources (~ 15) with apparently spurious colours (e.g. positive [J] - [H], negative [H] - [Ks]). This is consistent with the predicted number of mismatches in § 4.1. Inspection of their SED's reveals two distinct components: a steeply decreasing flux density at J and H band followed by an almost constant flux at Ks and above, as expected from mismatched sources. Visual inspection confirms this result. Apart from the possible mis-matched sources, there are very few stars with significant IR excess found using the J, H and Ks colours. The [J]-[Ks] vs [Ks] diagram shows sources are clustered at both

$\sim (0.7, 14)$ and $\sim (1.4, 12)$. However, the spatial positions of the sources clustered at these points in the CM diagram are evenly spread across the field.

To ensure these features were real (and as a further check on the automated star finding/photometry/matching processes), we repeated the above analysis using the 2MASS only and IRIS2 only PSCs. Both show the same features with spurious colours in the CC diagram and the clumping in the CM diagram.

Figure 9 shows selected CC diagrams including the 3.6 and $4.5\mu\text{m}$ sources. The combination of longer wavelengths and larger wavelength baselines in the [J]-[H] vs [Ks]-[4.5] CC diagram pulls out many more sources with IR excess, confirming that the JHKs colour combination is not ideal for this purpose. Although the wavelength baselines are smaller, each of the colours in the [H]-[Ks] vs [3.6]-[4.5] diagram are generated by measurements on the same instruments so instrument specific systematic offsets should be minimised. As in Figure 8 there are a number of sources with spurious colours. These are again consistent with mismatched sources.

5.1.1 IR excess sources

To identify the youngest sources we need to distinguish between stars with true IR excess and contaminating field stars with red colours due to extinction. We adopt the relationship derived by Indebetouw et al. (2005), who show that the extinction due to dust between 1.2 to $8\mu\text{m}$ is well fit with a single slope along several lines of sight within the galaxy. Figure 10 shows the [J] - [H] vs [Ks] - [4.5] CC diagram of stars matched in all four bands with two solid, non-vertical lines giving the reddening vectors of length $A_v=50$ mags. The field star population in the infrared is likely to be comprised mainly of giants but for completeness, colours for main-sequence and super-giant stars are also shown as the curved line between ([Ks]-[4.5],[J]-[H]) of $\sim (0,0)$ and $\sim (0,1)$ and the two reddening vectors start from the extremes of the sequences. Most of the stars lie within or close to these vectors and are therefore reddened rather than IR excess sources. As the relative photometric error increases with the measured magnitude, identifying sources with statistically significant IR excesses will depend on the source magnitude. However, applying magnitude limits to remove faint sources has little effect on the reddened sources in the diagram. We then use a statistical approach to determine which of the reddened sources are likely to be field stars as opposed to intrinsically red sources. Assuming the error in the colours is normally distributed, the number of field sources outside the reddening vectors should drop off given by the statistics of the normal distribution. The dashed line shows the reddening vector with a 3σ (0.6 mag) deviation from the main-sequence line which should encapsulate $\sim 99.7\%$ of the field sources. In this way, we can calculate the over-abundance of reddened sources at a given location in the colour-colour diagram and the likelihood that they are intrinsically reddened. We adopt a value of 3σ of the photometric derived in §2 to distinguish sources with IR excess and acknowledge a possible contamination of $\sim 0.3\%$ from the field source population.

Although CC diagrams are powerful tools of finding stars with IR excess, they can only pick stars matched

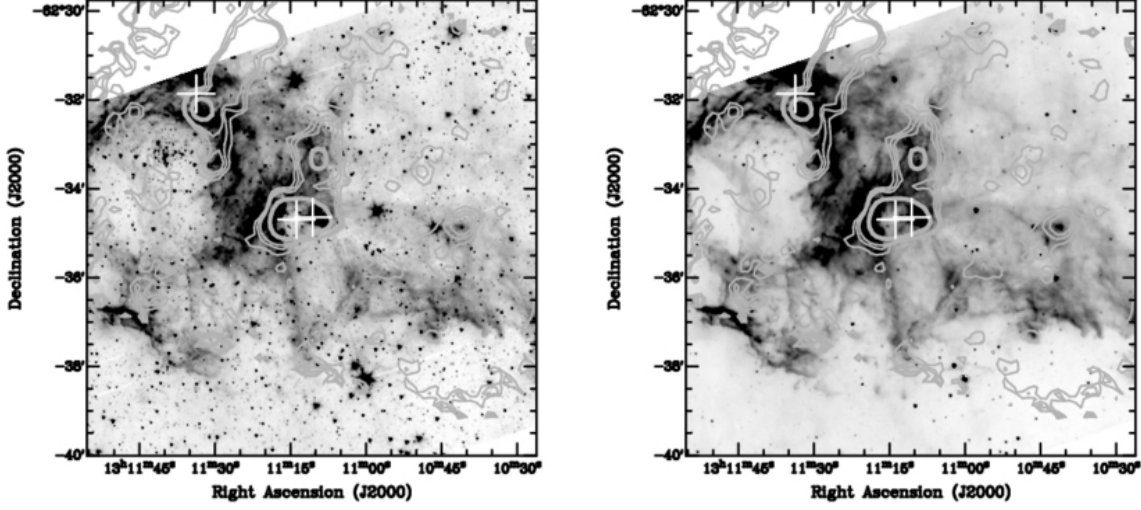


Figure 6. GLIMPSE 3.6 μ m (left) and 4.5 μ m (right) images of the region overlaid with the 5, 10, 15 and 50 σ 1.2mm continuum contour levels. The crosses show the position of the methanol maser emission.

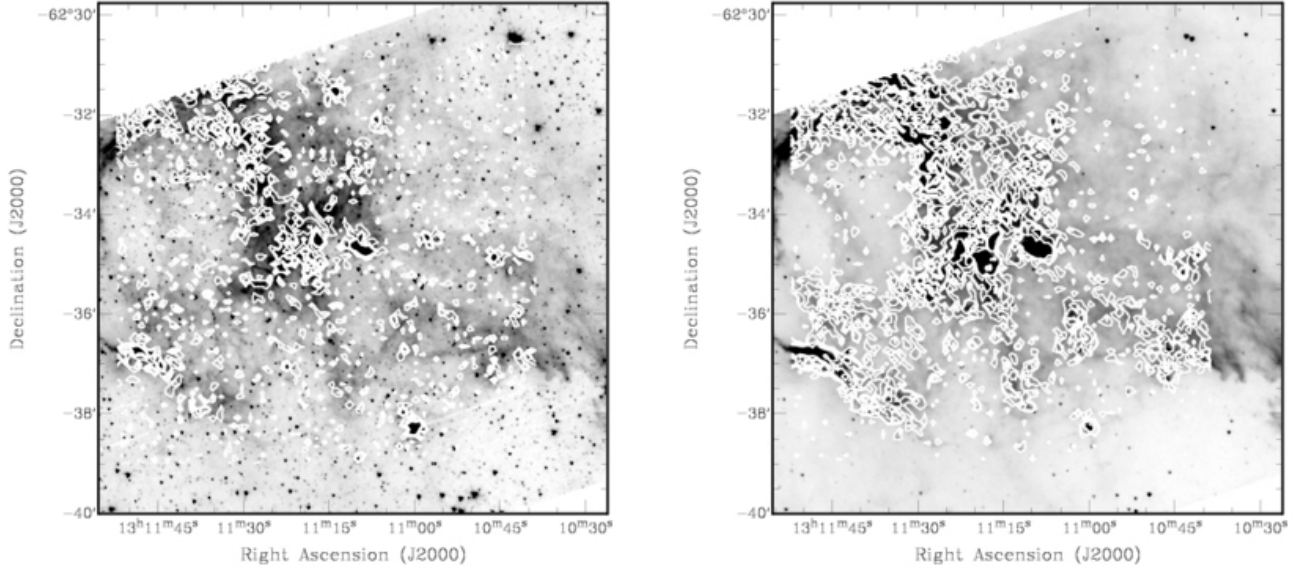


Figure 7. The spatial variation in completeness (see § 4.2) over the IRIS2 field of view at 3.6 (left) and 4.5 μ m (right) overlaid on the 3.6 μ m and 4.5 μ m GLIMPSE images. The contours show the relative completeness at -0.5, -1.0, -1.5 and -2.0 mags, highlighting the areas with poorest point source sensitivity.

at all the bands used to make the plot (i.e. from 1.2 to 4.5 μ m). This removes a large number of potentially highly reddened sources which are not detected at shorter wavelengths. The spectral index is defined in terms of frequency as, $n = d[\log(\nu F_\nu)]/d[\log(\nu)]$ or in terms of wavelength as $\alpha = d[\log(\lambda F_\lambda)]/d[\log(\lambda)]$ (where $n = -\alpha$) and gives the gradient of the IR spectral energy distribution. As a detection is only required at two frequencies, the spectral index provides a measure of source reddening which circumvents the requirement for sources to be observed at

all bands. Figure 11 shows a histogram of the spectral index of all sources matched at Ks and 4.5 μ m ($\alpha_{Ks-4.5}$). The top and central panels show the distribution in the control field (see §4.3) and target region respectively, for sources matched in the 2MASS/GLIMPSE PSC. Both peak at $\alpha_{Ks-4.5} \sim 2.5$ but the target region exhibits a strong tail of red sources compared to the symmetric distribution in the control region. The bottom panel shows sources matched in the IRIS2/GLIMPSE PSC of the target region. The distribution is similar to that found using the 2MASS/GLIMPSE

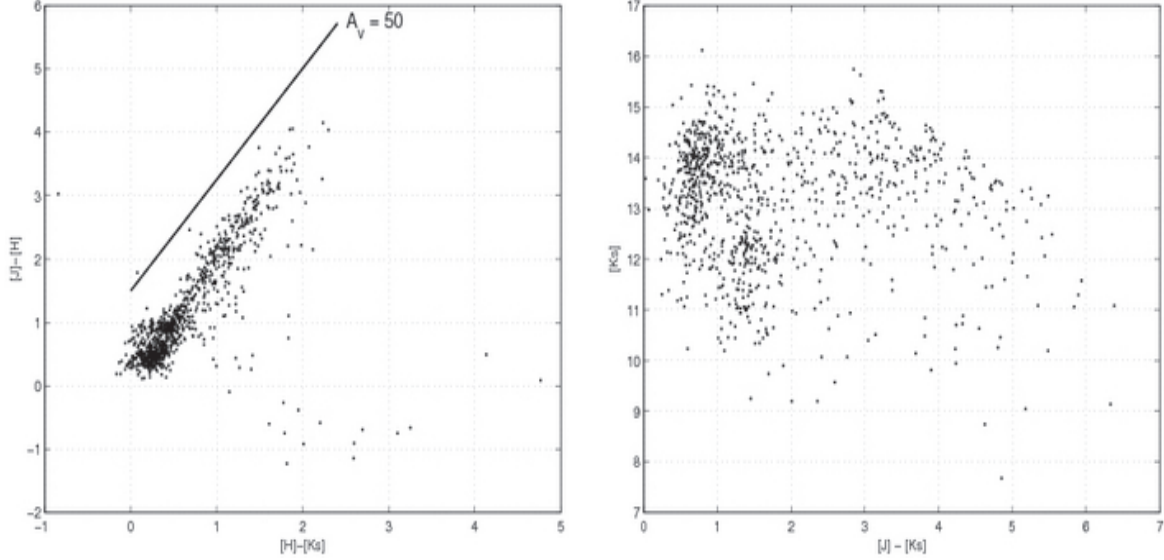


Figure 8. (Left) J, H, Ks colour-colour diagram of all stars in the IRIS2/GLIMPSE PSC matched in the IRIS2 J, H and Ks catalogues. The line gives the reddening vector with a visual extinction of 50 mags. Inspection of the sources with spurious colours ($[J] - [H] < 0$, $[H] - [Ks] > 0$) have been mismatched by the automated matching routine (§5.1). The number of mismatched sources is consistent with that predicted in §4.1. Very few IR excess sources are apparent at these wavelengths. (Right) J, Ks colour-magnitude diagram of all stars matched in the IRIS2 J, H and Ks catalogues. Although sources are clustered at both $\sim(0.7, 14)$ and $\sim(1.4, 12)$ in the CM diagram, the spatial positions of these sources are evenly spread across the field.

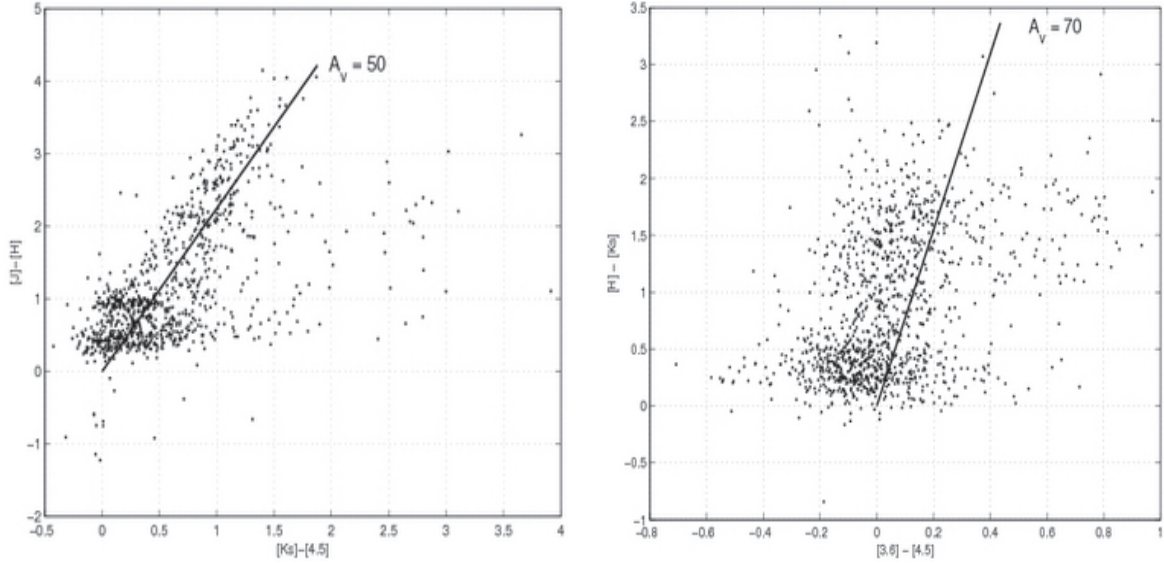


Figure 9. (Left) $[J] - [H]$ vs $[Ks] - [4.5]$ and (Right) $[H] - [Ks]$ vs $[3.6] - [4.5]$ colour-colour diagrams of stars matched in both the IRIS2 and GLIMPSE catalogues. The straight lines show the reddening vectors due to dust extinction, corresponding to $A_v = 50$ and 70 mags respectively.

PSC but even more red sources are detected due to the much deeper near-IR observations.

The spectral index in the near and mid-IR can also be used to infer the nature of the sources. Normally sources are divided based on the following criteria: $\alpha < -2$ as Class III, $-2 < \alpha < 0$ as Class II, $\alpha > 0$ as Class I with Class 0 unobservable in the IR (Adams et al. 1987; Wilking 1989). However, Figure 10 shows that there are a substantial fraction of highly reddened field stars in this region with spec-

tral indices in this range. To separate the highly reddened field stars from the embedded sources we first divide the full source population into three groups (Group I, II and III) with the same spectral index cuts used for Class I to III. Using the $[Ks] - [4.5]$ vs $[J] - [H]$ CC diagram (Figure 10) we can then investigate the likely field star contamination in each of the groups. The two vertical lines in Figure 10 show the position of stars with spectral indexes of $\alpha = -1.5$ (left) and 0 (right). Clearly, sources with $\alpha < -1.5$ are al-

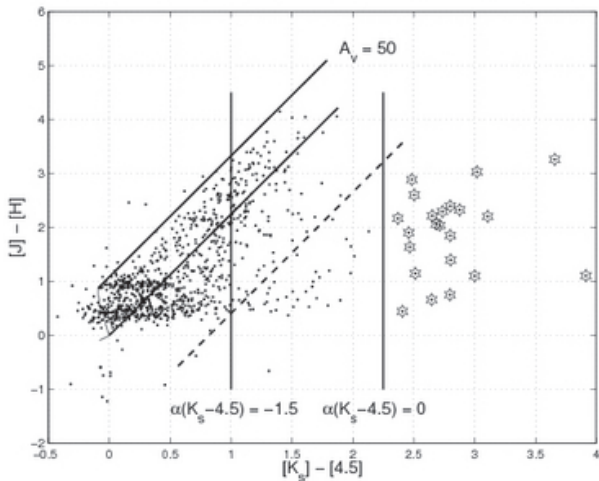


Figure 10. $[K_s]-[4.5]$ vs $[J]-[H]$ colour-colour diagram of stars matched in all four bands. Colours for main-sequence and super-giant stars are shown as the curved line between $([K_s]-[4.5], [J]-[H])$ of $\sim(0,0)$ and $\sim(0,1)$. The two solid, non-vertical lines are reddening vectors with $A_v=50$ mags. The upper line starts from the end of the super-giant branch $\sim(0,1)$ and the lower line starts from the main sequence $\sim(0,0)$. The dashed line shows the reddening vector with a 3σ deviation in the photometric error (see §2) from the main-sequence line (see § 5.1.1). All stars under the dashed line are classified as having an infrared excess. The two vertical lines show the position of stars with spectral indices, α , of -1.5 (left) and 0 (right). Sources marked with stars are those with $\alpha > 0$.

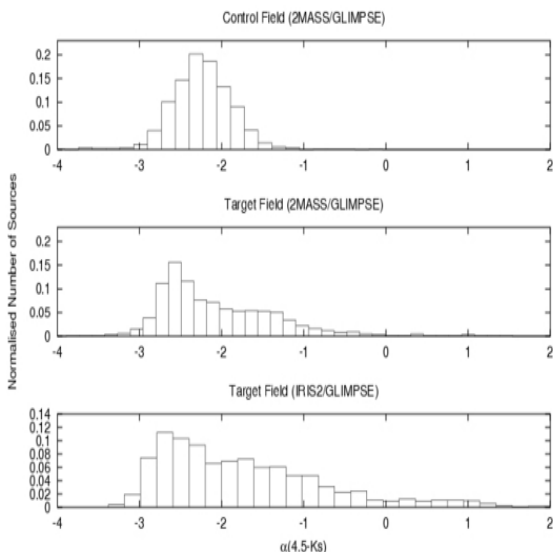


Figure 11. Histogram of the distribution of spectral indices ($\alpha = d[\log(\lambda F_\lambda)]/d[\log(\lambda)]$) for all sources matched at Ks and $4.5\mu\text{m}$. The top and central figures show the distribution in the control field (see §4.3) and target region respectively, for sources matched in the 2MASS/GLIMPSE PSC. The bottom figure gives the distribution of sources matched in the IRIS2/GLIMPSE PSC of the target region.

Spectral Index	Group	$N_{J-4.5}$	$N_{K-4.5}$	FS fraction
$\alpha < -1.5$	III	766 (82%)	899 (64%)	~ 1
$-1.5 < \alpha < 0$	II	147 (16%)	392 (28%)	~ 0.76
$0 < \alpha < 1.5$	I	20 (2%)	99 (7%)	< 0.002
$\alpha > 1.5$	Ie	2 (0.2%)	12 (0.9%)	-
Total		935	1402	

Table 1. Number of stars as a function of spectral index. The group names and spectral index selection is explained in § 5.1.1. $N_{J-4.5}$ are the number of stars in each of the groups which were matched in J, H, Ks and $4.5\mu\text{m}$ bands. Likewise, $N_{K-4.5}$ are the number of stars in each of the groups which were matched in Ks and $4.5\mu\text{m}$ bands only. The values in parentheses are the fraction of the total number of sources in each of the groups. The final column gives the approximate fraction of sources in each of the groups which are likely to be field stars rather than stars with intrinsic IR excess (as calculated in § 5.1.1).

most exclusively field stars. The $\alpha = -1.5$ line provides a much better cut than $\alpha = -2$ to separate the significant excess sources and is used from now on to define the cut off between Groups II and III. The large extinction ($A_v \sim 50$ mags) also means only 24% of the sources with $-1.5 < \alpha < 0$ are true IR excess sources – most are in fact just highly reddened field stars. The final selection of IR excess sources from the spectral index therefore only included sources with $\alpha > 0$ and those below the 3σ photometric error reddening vector.

Table 1 lists the number of stars in each of the groups found using spectral indexes of sources detected at all bands in two different wavelength ranges: the first from J to $4.5\mu\text{m}$ ($\alpha_{J-4.5}$) and the second from Ks to $4.5\mu\text{m}$ ($\alpha_{K-4.5}$). In total there are 50% more sources found using the Ks and $4.5\mu\text{m}$ bands. The fraction of Group II and I sources also increases substantially using the longer wavelengths. There are a number of Group I sources with extreme IR excess ($\alpha > 1.5$) which we define as Group Ie and are potentially even more embedded than the other Group I objects. Figure 12 plots the spectral energy distribution (SED) for each of the twelve Group Ie sources. With the exception of one source (number 8), the spectral index between Ks and $4.5\mu\text{m}$ is a good indication of the SED between 1.2 and $8\mu\text{m}$ in general. The fact that most of these 12 sources are not detected at 5.8 and/or $8.0\mu\text{m}$ confirms these would not have been good filter choices to pick out IR excess sources. Inspecting the SED's of sources in the other groups results in the same conclusion that the spectral index between Ks and $4.5\mu\text{m}$ is a good indication of the SED between 1.2 and $8\mu\text{m}$ in general. Figure 10 suggests it is highly unlikely that Group I sources are contaminated with field stars and these sources should therefore be equivalent to Class I embedded sources. However, care must be taken not to over-interpret the evolutionary stage from the SED alone as the geometry of these young sources must be, at minimum, two dimensional (Whitney et al. 2005). The measured colours/spectral indexes are also therefore dependent on the viewing angle.

The expected lifetime of Class I, II and III sources should be reflected in the relative number of sources in the different classes. For low mass stars these ages are around

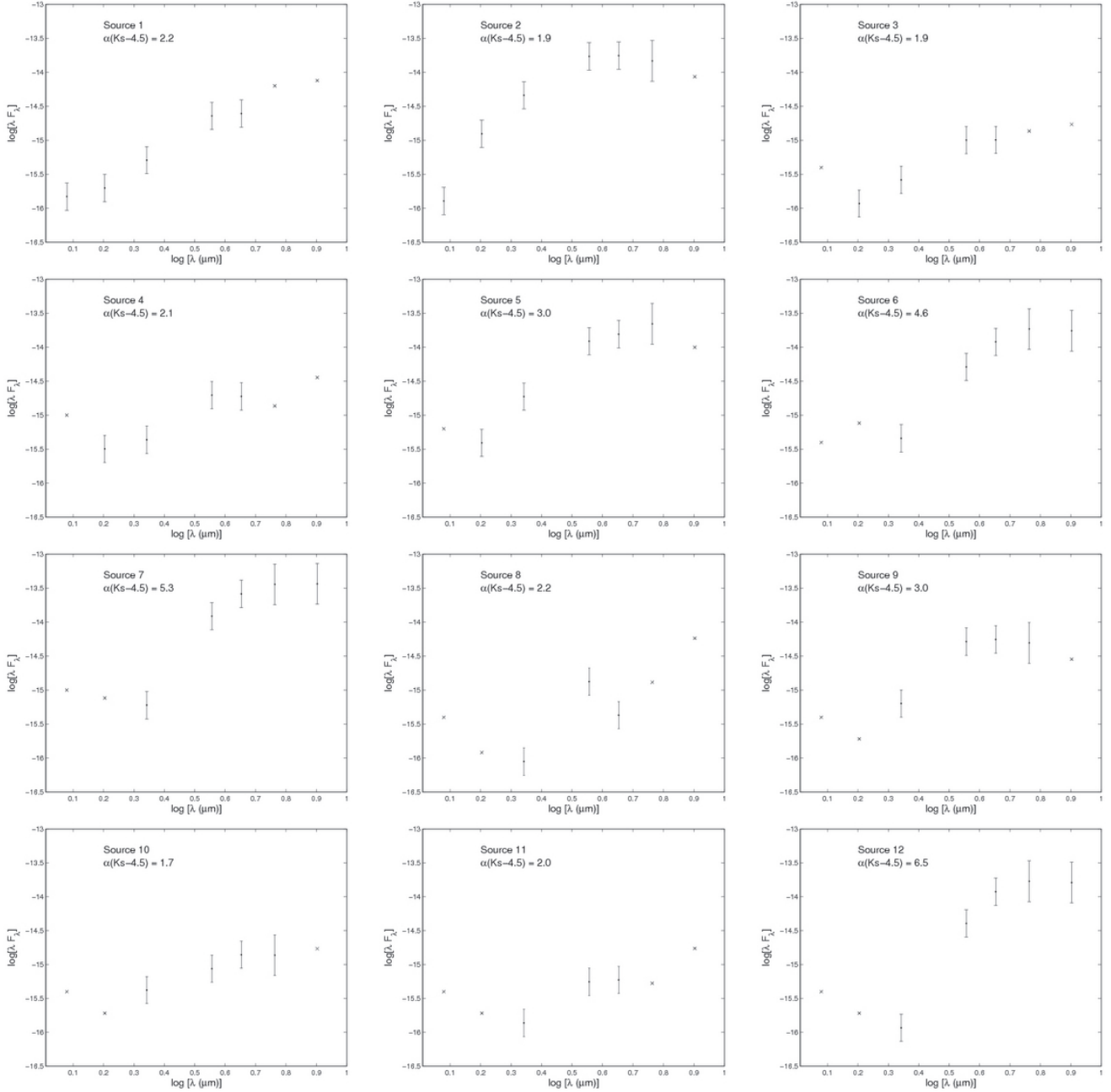


Figure 12. Spectral energy distributions for the twelve Group Ie sources (defined in §5.1.1 as sources with a spectral index between Ks and $4.5\mu\text{m}$ of greater than 1.5). The source number and spectral index calculated between Ks and $4.5\mu\text{m}$ are given as text for each source. The error bars shown are equal to the photometric accuracy of GLIMPSE and the IRIS2 images (see §2 & 3.2). For wavelengths with non-detections, crosses show the completeness magnitude within the nearest $5'' \times 5''$ pixel (as described in §4.2). It should be noted that these are only approximate upper limits due to the fairly coarse (0.5 mag) steps used and because the completeness is assumed to remain constant over each grid point. With the exception of source 8, the calculated spectral index between 2.2 & $4.5\mu\text{m}$ is in good agreement with the shape of the SED measured over the complete wavelength baseline.

10^5 , 10^6 and 10^7 years for Class I to III respectively (e.g. Lada (1999)). Although Figure 15 shows that the detected IR excess sources are likely to be more massive than this, these ages provide a strong upper limit as massive stars form much more quickly than their lower mass counterparts.

The significant field star contamination in Groups II and III provides a strong upper limit to the number of Class II and III sources. However, without an accurate source

count in each Class, an in-depth analysis is not possible. Assuming the age ratios of the observed IR excess sources are similar to the low mass case, there appears to be a large over-abundance of Class I sources (see Table 1). In any case, the much shorter formation timescales for the more massive stars suggests there has been a recent epoch of star formation within the region.

5.1.2 Spatial Distribution of Sources

Figure 13 shows the distribution of sources (as crosses) across the region based on their groups as determined from the spectral index between Ks and $4.5\mu\text{m}$ (described in §5.1.1). The contours show the median subtracted completeness at -0.5 mags for Ks (black) and $4.5\mu\text{m}$ (grey) highlighting areas of poorer point source sensitivity at each wavelength. For clarity, the $4.5\mu\text{m}$ completeness image was smoothed using a $15'' \times 15''$ kernel before generating the contours.

Before interpreting the spatial distribution of source colour, we first consider the effects of completeness as a function of wavelength across the region. The most obvious effect is that regions with few crosses correlate with those regions with poorest completeness. Investigation of the source colours in these regions, including the current sites of massive star formation (MM4 in Figure 1), will therefore be strongly biased by the completeness effects. Instead, we focus on the surrounding region in which the median subtracted completeness is > -0.5 mags at both Ks and $4.5\mu\text{m}$. Within this ‘moderate completeness’ region, completion effects will be small and comparable to the photometric error.

The top left, top right, bottom left and bottom right plots in Figure 13 give the spatial distribution of the Group III, II, I and Ie sources, respectively (as defined in §5.1.1). The Group III and II sources are fairly evenly distributed throughout the moderate completeness region. The clear exception is the density peak in the top right image, revealing that most of the G305.24+0.204 cluster members are Group II sources. Confusion due to stellar crowding in the cluster is the cause of the poorer completeness limit at Ks band in this region.

Interestingly, the Group I and Ie distributions shows a substantial number of IR excess sources lie offset from the known star formation regions (MM4 in Figure 1) in the moderate completeness region. Neither the Group I nor Ie sources are confined to a single area. The Group I sources in particular appear to be widely spread, with the exception of the two areas near $\alpha_{J2000}=13:11:35$, $\delta_{J2000}=-62:34:48$ and $13:10:49$, $-62:33:20$. Although much fewer in number, the 2MASS/GLIMPSE PSC of the region confirms these results and shows a similar source distribution.

Figure 14 shows the position of the Group I and Ie sources overlayed on the 1.2mm dust continuum emission. Several of the Group I sources in the IRIS2 field of view lie either completely outside the 1.2mm field or in regions of much poorer sensitivity within $60''$ of the 1.2mm field edge. As a result, these sources should be discarded from discussion involving the IR excess source distribution and the dust distribution. Of the remaining sources in the moderate completeness region, most are associated with, or lie close to, dust clumps.

5.2 Properties of the IR cluster G305.24+0.204

The cluster at $\alpha_{J2000}=13:11:39.4$, $\delta_{J2000}=-62:33:11.55$, designated G305.24+0.204 by Clark & Porter (2004) has previously been studied in detail at near-IR wavelengths by Leistra et al. (2005). With similar observations to Leistra et al. (2005), we first use the results of their spectroscopic analysis as a further check on our photometry and match-

ing algorithms in § 5.2.1, then discuss the interaction of the cluster with the surrounding environment in § 5.2.2 and finally investigate the embedded stellar populations using the longer wavelength data in § 5.2.3.

5.2.1 JHKs photometry

To analyse the cluster population we selected all stars within a radius of $45''$ of the cluster centre and a second control sample of stars within $45''$ of the position $\alpha_{J2000}=13:11:42.4$, $\delta_{J2000}=-62:34:32$. Figure 15 shows the [J]-[Ks] vs [Ks] colour-magnitude diagram of stars matched in the two bands. The stars near the cluster are shown as dots/triangles and the control stars as squares. The control stars and the stars in the cluster field not associated with the cluster are similarly spread throughout the diagram. The stars associated with the cluster are clearly concentrated at $([J]-[Ks], [Ks]) \sim (1.9, 13)$ which is consistent with O and B stars at a distance of 3.9kpc with an extinction of $A_v \sim 11$ mags. This is also consistent with previous distance estimates and calculated extinctions based on spectral identifications of the most luminous stars in the IR band (see Leistra et al. (2005)). The sources shown as triangles are those within the cluster region which lie to the red-ward side of the Main Sequence line defining the cluster members by $>3\sigma$ of the photometric error. These sources either do not belong to the cluster or are reddened cluster members. IR excess sources toward the cluster are discussed in §5.2.3.

5.2.2 Interaction with the surrounding environment

With powerful winds and radiation pressure driven by the OB stars, the cluster has the potential to interact strongly with the surrounding environment. Recent observations show there is diffuse 4GHz continuum associated with and surrounding the cluster (Walsh, private communication) which appears to be roughly confined by the surrounding extended emission seen in the infrared. It is plausible that the cluster of OB stars is therefore responsible for both ionising the surrounding region (evidenced as cm-continuum emission) and providing the UV flux exciting the PAH emission which surrounds the cluster (see Figure 7). A reasonable interpretation of this evidence is that the cluster is driving an expanding shell of molecular material into the surrounding region, the densest regions of which are observed as the 1.2mm dust continuum clumps. The fact that some of these clumps are in the earliest stages of forming stars (as indicated by the nearby methanol maser and Group Ie sources in the south-eastern peak of MM3 in Figure 1) suggests the cluster may have been responsible for triggering a further generation of star formation.

5.2.3 IR excess sources

Leistra et al. (2005) reported no IR excess stars toward the cluster from J, H and Ks colours. However, including the longer wavelength data reveals an over density of IR excess sources located around the cluster (Figure 16). Sources with $\alpha > 0$, based on the slope of the spectrum from Ks to $4.5\mu\text{m}$, are distributed around the core of the cluster but none are found at the centre. From Table 1 and the arguments in

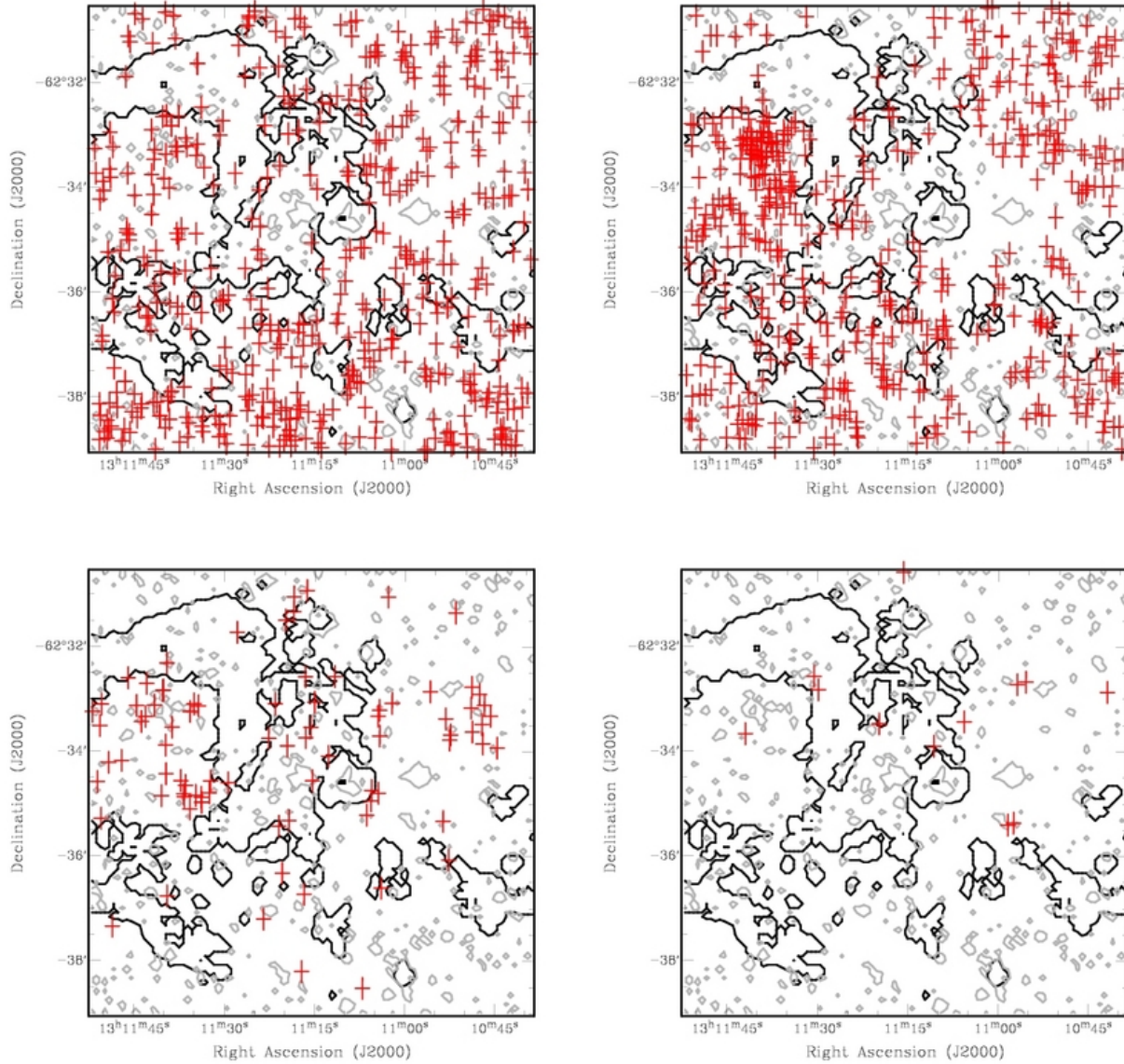


Figure 13. Source positions (shown as crosses) as a function of the spectral index between Ks and $4.5\ \mu\text{m}$, $\alpha(Ks - 4.5)$. The contours show the median subtracted completeness at -0.5 mags for Ks (grey) and $4.5\ \mu\text{m}$ (black) highlighting areas of poor point source sensitivity at each wavelength. For clarity, the $4.5\ \mu\text{m}$ completeness image was smoothed using a $15'' \times 15''$ kernel before generating the contours. Areas outside these contours are termed regions of ‘moderate completeness’. Source positions are separated into their respective groups (see §5.1.1 for details) as follows: Group III (top left), Group II (top right), Group I (bottom left) and Group Ie (bottom right).

§ 4.4, these are unlikely to be contaminating reddened field stars or background galaxies. Although there is no way to unambiguously confirm these sources belong to the cluster, it seems unlikely that $>15\%$ of the IR excess sources in the entire region would randomly fall within $<5\%$ of the total area (corresponding to a radius of $60''$) of a randomly chosen location. While this is certainly not a rigorous argument (it is biased by our selection of the radius around the cluster for example) it provides reasonable justification for assuming that at least some of these sources are associated with the cluster. In this case, can we find an explanation for the lack of IR excess objects towards the cluster centre?

Figure 16 shows that confusion due to the high stellar density towards the cluster centre at Ks leads to significantly

poorer completion limits at this wavelength. It is therefore possible that by using the spectral index between Ks and $4.5\ \mu\text{m}$, real IR excess sources detected at $4.5\ \mu\text{m}$ toward the cluster centre have been missed as they lie beneath the Ks completion limit. Figure 16 illustrates that the completeness problem drops substantially at $3.6\ \mu\text{m}$ and is almost non-existent toward the cluster centre at $4.5\ \mu\text{m}$. Therefore, to investigate the apparent lack of IR excess sources toward the cluster centre, we used the GLIMPSE only catalogue of the region. This removes any potential errors due to the automated photometry and matching caused by the high stellar crowding in the IRIS2 images. In the GLIMPSE PSC, all of the sources detected at $4.5\ \mu\text{m}$ towards the cluster were also detected at $3.6\ \mu\text{m}$, despite the reduced completeness in

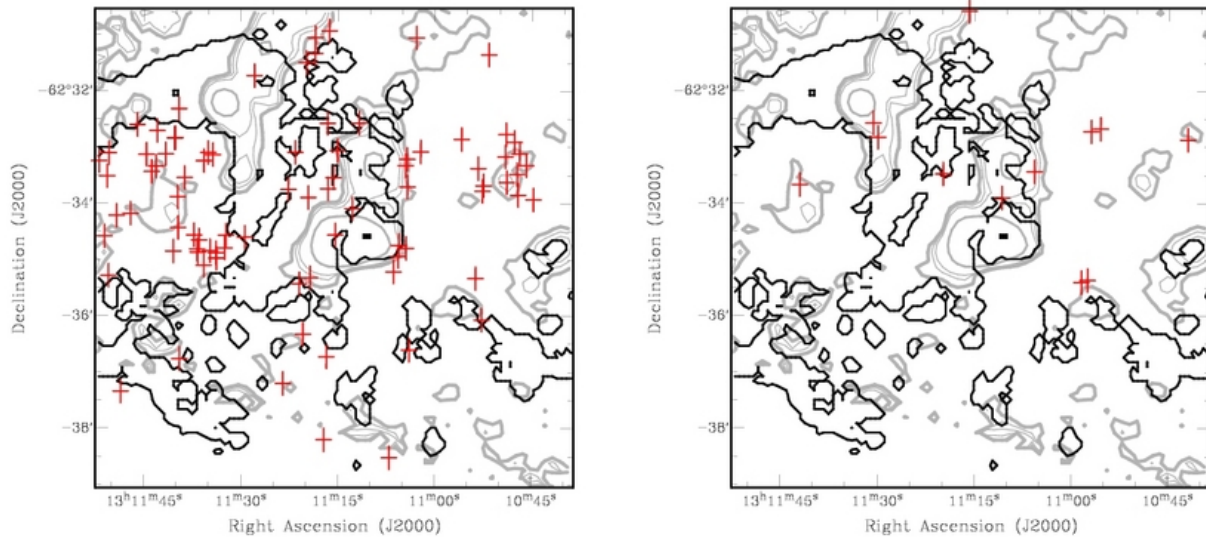


Figure 14. Source positions (shown as crosses) as a function of the spectral index between Ks and $4.5 \mu\text{m}$, $\alpha(Ks - 4.5)$, for Group I (left) and Group Ie (right) sources. The grey contours show the 1.2mm continuum emission at 5, 10, 15 and 50σ . The black contours show the -0.5 magnitude median subtracted completeness at $4.5\mu\text{m}$. For clarity, the $4.5\mu\text{m}$ completeness image was smoothed using a $15'' \times 15''$ kernel before generating the contours.

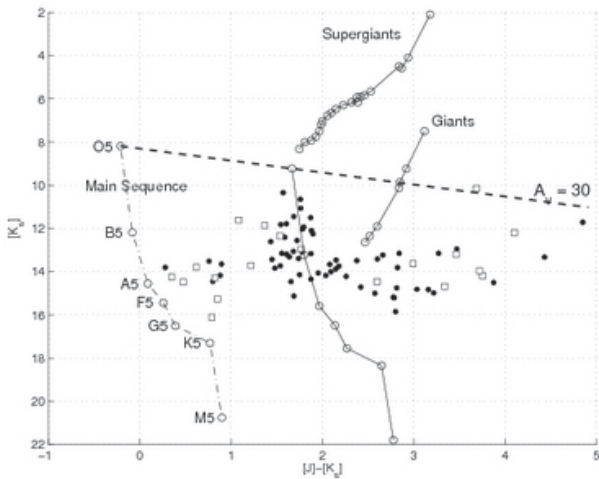


Figure 15. $[J]-[Ks]$ vs $[Ks]$ colour-magnitude diagram of stars matched in the two bands within a radius of $45''$ from the cluster centre ($\alpha_{J2000}=13:11:39.4$, $\delta_{J2000}=-62:33:12$), shown as solid dots. The squares show stars within the control region, also of radius $45''$. The control and cluster sources have a similar distribution with the exception of the clear over abundance of sources in the cluster field between $[J]-[Ks]$ of 1.5 to 2.3. The dot-dashed line shows the position of the Main Sequence and selected stellar spectral types as open circles, with no reddening, at a distance of 3.9kpc (the distance to the central star forming region). The dashed line shows a reddening vector with a length of $A_v=30$ mags. The solid lines show the position of the Main Sequence, Giant and Supergiant stars at 3.9kpc with $A_v=11$ mags with open circles again showing selected spectral types. The majority of stars in the cluster field (solid circles) lie along this Main Sequence as O or B stars.

the $3.6\mu\text{m}$ images. As the $4.5\mu\text{m}$ image does not suffer from reduced point source sensitivity towards the cluster centre (see Figure 16), we conclude that we have a complete sample of $4.5\mu\text{m}$ sources for the cluster. The spectral index between 3.6 and $4.5\mu\text{m}$ from the GLIMPSE PSC confirms the lack of IR excess sources toward the cluster centre and again shows IR excess sources at the cluster edge.

The previous analysis has been based on the major assumption that the IR excess sources belong to the cluster. Besides their proximity, is there any reason to believe they may be associated? In comparison to the Orion Nebula Cluster (ONC), these stars are slightly outside the radius of $\sim 0.2\text{pc}$ of the stars in the Trapezium which form the core of the ONC (Hillenbrand & Hartmann 1998). However, they are well inside the $\sim 2.5\text{pc}$ radius comprising the entire ONC (Hillenbrand 1997), which has in excess of a thousand members visible in the near-IR. Using the ONC for comparison, it seems plausible that the IR excess sources could belong to a larger complex based around the cluster.

6 DISCUSSION

With an indicator of the source ages and their spatial distribution, we can investigate the star formation history of the G305.2+0.2 region. Although we cannot probe the most heavily embedded regions due to incompleteness, the question remains – how did the detected IR excess sources form in a short period ($\leq 10^6$ years) over such a large distance ($\sim 5 \text{ pc}$) and yet are clearly separated from the known regions of star-formation activity, such as the UCHII regions and maser emission toward MM4? If these are the only sites of recent star formation, one possible explanation may be that the IR excess sources have been ejected from them. To investigate the plausibility of this argument, we consider the angular distance on the sky it is feasible for a star at a

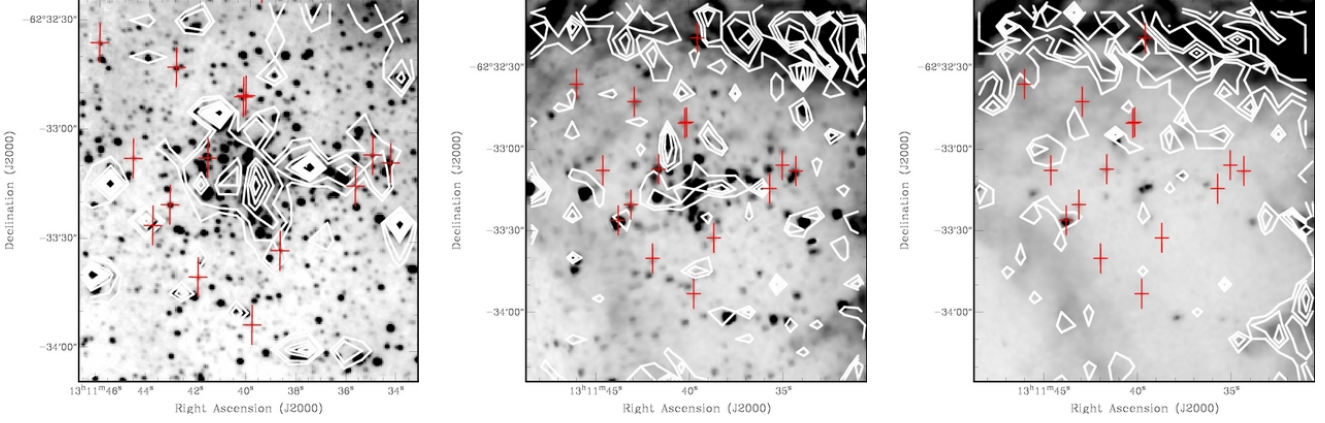


Figure 16. Images at Ks (left), $3.6\mu\text{m}$ (centre) and $4.5\mu\text{m}$ (right) of the IR cluster G305.24+0.204. The contours show the median subtracted completeness at each wavelength in steps of -0.5 magnitudes, highlighting areas with poorer point source sensitivity. Crosses show the position of IR excess sources ($\alpha(\text{Ks}-4.5) > 0$, group I and Ie) within $60''$ of the cluster centre.

distance of 3.9kpc to have moved within its lifetime. Hoogerwerf et al. (2000, 2001) show that 10% of massive stars are high velocity ($> 30\text{ km s}^{-1}$) runaways and up to 30% are moderate velocity ($10 < V < 30\text{ km s}^{-1}$) runaways. A class I star with a lifetime of 10^5 years and an ejection velocity of $\sim 10\text{ km s}^{-1}$ could therefore potentially have travelled an angular distance of $60''$ ($\sim 1\text{pc}$) at 3.9kpc .

Huff & Stahler (2006) argue that local potential wells caused by other stars and ambient molecular gas will stop stars drifting from the cluster on ballistic trajectories. However, in young, massive, Trapezium-like systems with stellar densities $\sim 10^4\text{pc}^{-3}$ (Hillenbrand 1997) and large numbers of companions per system, dynamical ejections are likely. The potential due to other stars and even molecular gas is not sufficient to stop the ejection as evidenced by an ejection event within the last 500 years in the deeply embedded BN-KL complex in Orion, which produced a runaway OB star (Rodríguez et al. 2005). If the IR excess objects we observed have been ejected, measurement of their proper motion vectors with milliarcsecond astrometry over a decade long time scale should reveal whether they are indeed moving at several km s^{-1} away from the sites of active star formation. However, while this is certainly plausible for some sources, particularly those nearest MM4, it seems unlikely that this can account for all the IR excess sources. The shorter lifetimes of high mass stars compared to their lower mass counterparts suggest an unreasonably high velocity for the sources farthest away from MM4. There is also no explanation for the non-homogenous ejections resulting in the two concentrations of IR excess sources.

Ruling out MM4 as the sole origin of the IR excess sources implies there must be other sites of recent star formation within the region. Focusing on regions with moderate completeness limits (see §5.1.2), the area confined by the PAH emission in the 3.6 and $4.5\mu\text{m}$ images stands out with a high density of IR excess sources (see Figure 13). The concentration of IR excess sources near $\alpha_{\text{J2000}}=13:11:35$ $\delta_{\text{J2000}}=-62:34:48$ and $13:10:49$ $-62:33:20$ make these strong candidates for sites of recent star formation. Interestingly, only the latter of these concentrations is associated directly with a dust core (MM7). This suggests it has not yet had

time to disperse its natal molecular material and, as such, may be the younger of the two sites. While IR excess sources are seen towards other dust cores in the moderate completeness region (MM6, MM8, the north-west of MM3 and the western side of MM5) the fewer sources numbers make the case for these regions less clear. Finally, the much poorer sensitivity at the edge of the 1.2mm field makes it difficult to comment on the association of IR excess sources with the dust in these regions.

7 CONCLUSIONS

We have generated a point source catalogue towards the G305.2+0.2 region from 1.2 to $8.0\mu\text{m}$ by combining deep, near-IR, IRIS2 images with catalogued mid-IR data. Modeling of the automated photometric extraction and star matching algorithms predicts a maximum of 0.12% mismatches in the catalogue, which is consistent with the number of sources with apparently spurious SED's. Through comparison with previous spectroscopic observations of the region we have confirmed the accuracy of the photometry. We find:

- There is strong extended PAH emission in the GLIMPSE images. This has the effect of significantly lowering the point source sensitivity in these regions, particularly at 5.8 and $8.0\mu\text{m}$. As a result we may be missing a population of the most heavily embedded sources, including those toward the known sites of massive star formation.
- 12 of the sources have extreme IR excess with spectral indices between $2.2\mu\text{m}$ and $4.5\mu\text{m}$ > 1.5 which we designate Group Ie. Analysis of the full SED shows the spectral index over this reduced wavelength range is a reliable indicator of the IR SED in general.
- The effect of the winds and radiation from the OB association G305.24+0.204 may be responsible for triggering a third generation of star formation.
- There is a population of IR excess stars surrounding the cluster G305.24+0.204 and an absence of such sources in the cluster centre. There is reasonable evidence that some

of these excess sources belong to the cluster. We discuss possible causes for this.

- There is a sizable population of IR excess sources offset from the known star formation sites. Analysis of these sources reveal multiple new sites of recent star formation. The formation activity in the G305.2+0.2 region is therefore much more widespread than previously thought.

8 ACKNOWLEDGEMENTS

We would like to thank Stuart Ryder for his help with the data reduction and Andrew Walsh for discussions of the G305 region. SNL would like to thank Charlie Lada, Lori Allen, Luisa Rebull and Rob Gutermuth for help interpreting GLIMPSE data. We thank the anonymous referee for instructive comments which significantly improved the clarity of the manuscript. SNL is supported by a scholarship from the School of Physics at UNSW. This research has made use of NASA's Astrophysics Data System.

REFERENCES

- Adams F. C., Lada C. J., Shu F. H., 1987, *ApJ*, 312, 788
- Benjamin R. A., Churchwell E., Babler B. L., Bania T. M., Clemens D. P., Cohen M., Dickey J. M., Indebetouw R., Jackson J. M., Kobulnicky H. A., +10 authors 2003, *PASP*, 115, 953
- Blum R. D., Mould J. R., Olsen K. A., Frogel J. A., Werner M., Meixner M., Markwick-Kemper F., Indebetouw R., Whitney B., Meade M., +40 co-authors 2006, *AJ*, 132, 2034
- Clark J. S., Porter J. M., 2004, *A&A*, 427, 839
- De Buizer J. M., 2003, *MNRAS*, 341, 277
- Dutra C. M., Bica E., Soares J., Barbuy B., 2003, *A&A*, 400, 533
- Fazio G. G., Ashby M. L. N., Barmby P., Hora J. L., Huang J.-S., Pahre M. A., Wang Z., Willner S. P., Arendt R. G., Moseley S. H., Brodwin M., Eisenhardt P., Stern D., Tollestrup E. V., Wright E. L., 2004, *ApJS*, 154, 39
- Georgelin Y. M., Boulesteix J., Georgelin Y. P., Le Coarer E., Marcelin M., 1988, *A&A*, 205, 95
- Groenewegen M. A. T., 2006, *A&A*, 448, 181
- Gutermuth R. A., 2005, PhD thesis, University of Rochester, United States – New York
- Hill T., Burton M. G., Minier V., Thompson M. A., Walsh A. J., Hunt-Cunningham M., Garay G., 2005, *MNRAS*, 363, 405
- Hillenbrand L. A., 1997, *AJ*, 113, 1733
- Hillenbrand L. A., Hartmann L. W., 1998, *ApJ*, 492, 540
- Hoogerwerf R., de Bruijne J. H. J., de Zeeuw P. T., 2000, *ApJL*, 544, L133
- Hoogerwerf R., de Bruijne J. H. J., de Zeeuw P. T., 2001, *A&A*, 365, 49
- Huff E. M., Stahler S. W., 2006, *ApJ*, 644, 355
- Indebetouw R., Mathis J. S., Babler B. L., Meade M. R., Watson C., Whitney B. A., Wolff M. J., Wolfire M. G., Cohen M., Bania T. M., co authors ., 2005, *ApJ*, 619, 931
- Jackson T., Ivezić Ž., Knapp G. R., 2002, *MNRAS*, 337, 749
- Kenyon S. J., Hartmann L., 1995, *ApJS*, 101, 117
- Lada C. J., 1999, in Lada C. J., Kylafis N. D., eds, *NATO ASIC Proc. 540: The Origin of Stars and Planetary Systems The Formation of Low Mass Stars: An Observational Overview*. pp 143–+
- Lada C. J., Adams F. C., 1992, *ApJ*, 393, 278
- Leistra A., Cotera A. S., Liebert J., Burton M., 2005, *AJ*, 130, 1719
- Longmore S. N., Burton M. G., Minier V., Walsh A. J., 2006, *MNRAS*, 369, 1196
- Maercker M., Burton M. G., 2005, *A&A*, 438, 663
- Maercker M., Burton M. G., Wright C. M., 2006, *A&A*, 450, 253
- Norris R. P., Whiteoak J. B., Caswell J. L., Wieringa M. H., Gough R. G., 1993, *ApJ*, 412, 222
- Phillips C. J., Norris R. P., Ellingsen S. P., McCulloch P. M., 1998, *MNRAS*, 300, 1131
- Rodríguez L. F., Poveda A., Lizano S., Allen C., 2005, *ApJL*, 627, L65
- Skrutskie M. F., Cutri R. M., Stiening R., Weinberg M. D., Schneider S., Carpenter J. M., Beichman C., Capps R. e., 2006, *AJ*, 131, 1163
- van Dishoeck E. F., 2004, *ARAA*, 42, 119
- Walsh A. J., 2002, in Migenes V., Reid M. J., eds, *IAU Symposium G305.20+0.21: A very young class II methanol maser source*. pp 155–+
- Walsh A. J., Bertoldi F., Burton M. G., Nikola T., 2001, *MNRAS*, 326, 36
- Walsh A. J., Burton M. G., 2006, *MNRAS*, 365, 321
- Whitney B. A., Robitaille T. P., Indebetouw R., Wood K., Bjorkman J. E., Denzmore P., 2005, in Cesaroni R., Felli M., Churchwell E., Walmsley M., eds, *IAU Symposium 2-D and 3-D radiation transfer models of high-mass star formation*. pp 206–215
- Willing B. A., 1989, *PASP*, 101, 229

Table 2. Example extract from the first five lines of the online catalogue of the sources matched between the IRIS2 J, H and Ks band images and the GLIMPSE point source catalogue. The first two columns give the source right ascension and declination in decimal degrees. Columns 3 to 11 give the magnitude, magnitude error and ID number of the sources at J, H and Ks band. Columns 12 through 19 give the magnitude and magnitude error of the sources at 3.6, 4.5, 5.8 and 8.0 μm from the GLIMPSE point source catalogue. The final column gives the GLIMPSE ID number. In this example table, the magnitudes and errors have been rounded to 2 decimal places for clarity. A value of ‘null’ means no source was detected at that wavelength.

RA J2000 (degrees)	Dec. J2000 (degrees)	J (mag)	ΔJ (mag)	ID (J)	H (mag)	ΔH (mag)	ID (H)	Ks (mag)	ΔKs (mag)	ID Ks	3.6 (mag)	$\Delta 3.6$ (mag)	4.5 (mag)	$\Delta 4.5$ (mag)	5.8 (mag)	$\Delta 5.8$ (mag)	8.0 (mag)	$\Delta 8.0$ (mag)	GLIMPSE ID
197.8149	-62.65503	15.90	0.02	372	14.12	0.01	522	13.27	0.01	13	12.71	0.09	12.57	0.10	null	null	null	null	13
197.7037	-62.65393	15.36	0.02	393	14.56	0.03	544	14.48	0.02	33	14.08	0.14	13.81	0.14	null	null	null	null	33
197.8973	-62.65512	14.20	0.02	388	13.02	0.04	542	12.36	0.03	39	12.12	0.08	12.08	0.07	null	null	null	null	39
197.916	-62.65464	18.41	0.12	433	16.29	0.04	596	15.16	0.03	82	13.95	0.14	13.89	0.29	null	null	null	null	82
197.7169	-62.65399	17.30	0.07	403	15.14	0.05	543	14.06	0.02	32	13.29	0.01	13.03	0.20	null	null	null	null	32